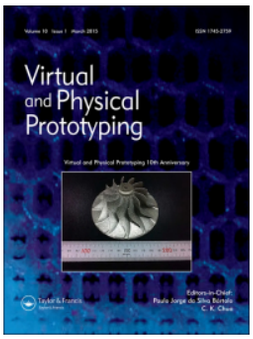

Taylor & Francis
Taylor & Francis Group

Virtual and Physical Prototyping

ISSN: 1745-2759 (Print) 1745-2767 (Online) Journal homepage: www.tandfonline.com/journals/nvpp20

Single-process 3D-printed smart pad with CNN-based touch localization and force classification

Tibor Barši Palmić, Enej Podlipnik & Janko Slavič

To cite this article: Tibor Barši Palmić, Enej Podlipnik & Janko Slavič (2026) Single-process 3D-printed smart pad with CNN-based touch localization and force classification, Virtual and Physical Prototyping, 21:1, e2640277, DOI: 10.1080/17452759.2026.2640277

To link to this article: https://doi.org/10.1080/17452759.2026.2640277

Published online: 31 Mar 2026.

VIRTUAL AND PHYSICAL PROTOTYPING
2026, VOL. 21, NO. 1, e2640277 (15 pages)
https://doi.org/10.1080/17452759.2026.2640277

Taylor & Francis
Taylor & Francis Group

Single-process 3D-printed smart pad with CNN-based touch localization and force classification

Tibor Barši Palmić, Enej Podlipnik and Janko Slavič

Faculty of Mechanical Engineering, University of Ljubljana, Ljubljana, Slovenia

ABSTRACT

Multi-material 3D-printing enables the single-process embedding of piezoresistive sensors producing multi-functional, fully 3D-printed, smart structures without manual assembly or specialized equipment. However, the low sensitivity and manufacturing variability yield unreliable signals, limiting 3D-printed sensors to simple demonstrations rather than complex sensing tasks. This work introduces a single-process, 3D-printed structure with inherently poor sensing capability that is transformed into a highly accurate smart pad with functional tap localization using a convolutional neural network (CNN). The structure consists of a thermoplastic polyurethane (TPU) pad with up to four embedded piezoresistive sensors fully fabricated through material extrusion (MEX). The CNN processes measured time-series signals to predict the tap location and classify the force magnitude. The 4-sensor smart pad reliably distinguishes individual taps with millimeter accuracy (3.56 mm mean accuracy), enabling touch-pad applications with force classification (>98.7% accuracy). The single-sensor smart pad maintains functional performance (6.32 mm mean accuracy), proving that machine learning compensates for the extreme sensor reduction. This work establishes a rapid-prototyping platform for application-specific CNN-enhanced smart structures in human-machine interfaces, soft robotics, and structural health monitoring.

ARTICLE HISTORY
Received 30 October 2025
Accepted 24 February 2026

KEYWORDS
Multi-material 3D-printing; smart structures; piezoresistive sensors; convolutional neural networks; impact detection

1. Introduction

Additive manufacturing (AM) has revolutionised the fabrication of custom geometries with unprecedented design freedom and rapid-prototyping capabilities [1, 2]. However, these structures typically remain passive, lacking integrated sensing and decision-making capabilities that would enable their intelligent functionality.

Multi-material 3D printing enables sensor embedding during fabrication, eliminating post-manufacturing assembly and reducing the system's complexity [3, 4]. Various sensing modalities have been demonstrated, including force [5], pressure [6], strain [7], acceleration [8], and tactile sensing [9], using piezoresistive [10], capacitive [11], and piezoelectric [12] mechanisms. However, sensors fabricated through material extrusion (MEX) in a single process exhibit fundamental limitations: low sensitivity, high noise-to-signal ratios, and poor repeatability due to manufacturing variability [13, 14]. Ongoing research is addressing these limitations across multiple fronts: material design through novel conductive composites [15], process optimisation via ironing and void reduction [16], and sensor-geometry tailoring [17].

Recently, the potential applicability of integrated smart structures, fully 3D-printed in a single process, has been demonstrated. Stano et al. [18] achieved the one-shot AM of a bio-inspired robotic finger with embedded shape-memory alloy actuators and integrated 3D-printed sensors, producing structures that provide real-time feedback immediately after their removal from the build plate. Zolfagharian et al. [19] presented a framework for closed-loop, 4D-printed soft robots integrating sensors and actuators for autonomous operation. Although the functional integration of 3D-printed systems has been demonstrated, the examples are few and often rely on custom processes and materials. More research is required to progress 3D-printed smart systems into real-world applications.

Touch or tap detection represents a demanding benchmark for evaluating 3D-printed sensing capabilities. Conventional systems achieving millimeter-scale localisation accuracy employ multiple, distributed sensors: 6–8 piezoelectric sensors for physics-based

CONTACT Janko Slavič janko.slavic@fs.uni-lj.si Faculty of Mechanical Engineering, Aškerčeva 6, 1000 Ljubljana

triangulation [20, 21], 2–8 sensors for machine-learning approaches as demonstrated by Damm et al. [22] and Li et al. [23], and 30+ sensors for large structures or enhanced spatial resolution [24, 25]. These systems require high-speed, multi-channel, data-acquisition hardware for simultaneous signal capture [26], post-manufacturing sensor installation [27], and calibration protocols under controlled conditions [28]. Conventional signal-processing methods – wave mechanics, time-of-arrival, and correlation-based approaches – require precise material characterisation, high signal-to-noise ratios, or stable baseline measurements: conditions unmet by 3D-printed sensors.

Deep learning overcomes these limitations by learning robust features directly from the data without requiring any material characterisation or precise physical models. Kiranyaz et al. [29] provided a comprehensive review of 1D convolutional neural networks (CNNs) for time-series applications, demonstrating their effectiveness across signal-processing domains, including structural health monitoring. These networks extract patterns from entire signal waveforms, inherently handling wave dispersion, measurement noise, and material variability. Attention-enhanced 1-dimensional CNN architectures prove effective for time-series sensor data [30], with Xu et al. [31] introducing temporal and channel attention mechanisms for dynamic feature extraction. Alternative machine-learning methods – support vector machines offering computational efficiency [23, 24] and traditional artificial neural networks with simpler architectures [32, 33] – have also been applied, though CNNs achieve superior accuracy exceeding 99% as reported by Damm et al. [22] and Migot et al. [34].

Achieving functional smart structures through single-process additive manufacturing remains challenging: 3D-printed sensors offer fabrication simplicity but produce low-quality signals unsuitable for demanding tasks like touch localisation. CNNs compensate for poor sensor quality by learning directly from noisy, variable responses without requiring precise material characterisation. Neither technology alone solves the challenge – 3D-printed sensors without intelligent processing remain too unreliable, while CNNs without embedded sensors require conventional hardware. The combination enables functional smart structures from minimal hardware.

This work introduces a single-process, 3D-printed smart pad with up to four piezoresistive sensors where CNN-based localisation and force classification achieve performances competitive with conventionally manufactured devices (comparison presented in Appendix 3). A compact CNN processes time-series signals to simultaneously predict the tap location and classify the force magnitude; sensor reduction experiments quantify the trade-off between the hardware simplicity and the localisation accuracy. The remainder of this paper is organised as follows: Section 2 presents the design and fabrication of the 3D-printed sensing structure, the experimental data-acquisition protocol, and the CNN architecture; Section 3 presents impact localisation and force classification results; and Section 4 discusses the implications and future research directions.

2. Methods

The methodology combines single-process additive manufacturing with machine learning to transform a simple structure into a functional sensing system. First, the design and the fabrication process with commercially available materials and technology are presented Section 2.1. Second, the experimental system and data acquisition are presented Section 2.2. Finally, the CNN architecture and learning strategy are explained Section 2.3. All the data, including the model and datasets, are publicly available on GitHub [35] for full reproducibility.

2.1. 3D-printed structure

The self-sensing structure consists of a single-process, 3D-printed flexible plate with four integrated piezoresistive strain sensors embedded in corner supports Figure 1(a). The overall plate dimensions including the rigid frame are 250 mm × 250 mm, with a suspended sensing region of 100 mm × 100 mm. Each of the four corner supports contains an embedded strain-sensing element that deforms during the touch or tap events.

The piezoresistive sensors feature a U-shaped geometry with both contact ends terminating in the frame to facilitate electrical connections (see Figure 1(b)). Each sensor has a cross-sectional area of $5 \times 1.25 = 6.25\,\text{mm}^2$ and an active sensing length of 94 mm. The nominal resistance of each sensor is approximately 1200 Ω, measured at zero strain.

Four sensors positioned at the edges of the plate capture the global structural response as elastic waves propagate from any impact location to the boundaries. Corner mounting maximises the strain concentration during the plate's deformation, enhancing sensor signal's amplitude. Tap events on the plate's surface generate elastic waves that propagate through the structure, inducing strain in the flexible corner supports where the piezoresistive sensing elements are embedded. The conductive TPU sensing elements exhibit piezoresistive behaviour, whereby strain

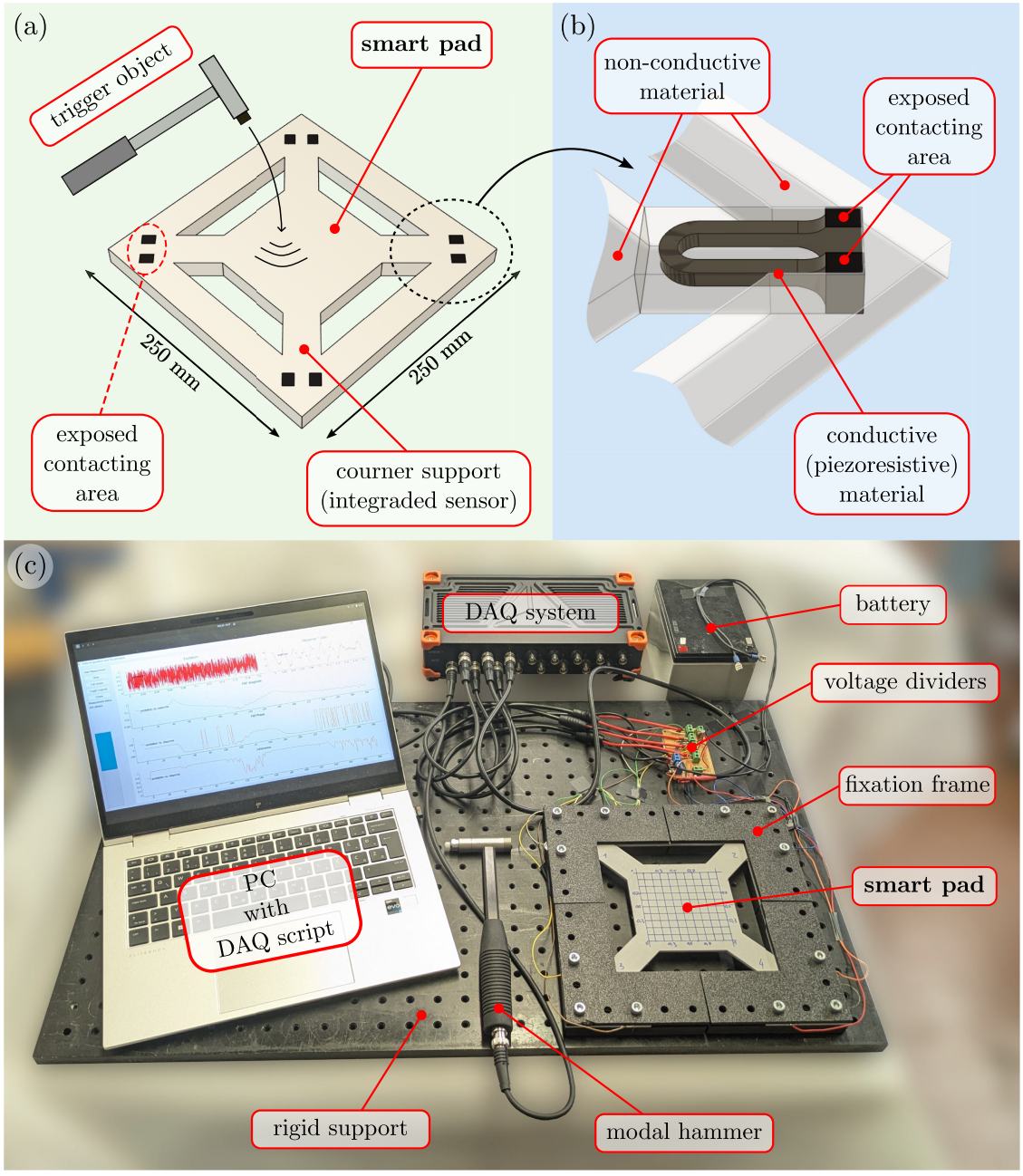

Figure 1. Schematic drawings of: (a) the 3D-printed smart pad with integrated sensors and (b) the integrated piezoresistive sensor. (c) Experimental setup for acquisition of training dataset with the 3D-printed smart pad mounted to the rigid support and all required equipment.

changes the electrical resistance, which is measured as a voltage using a voltage-divider circuit. Four simultaneous time-series voltage signals capture the dynamic structural response to each tap. The complex wave propagation, dispersion, and boundary reflections create unique signal signatures that encode the impact location and force magnitude, which the CNN learns to decode.

The plate's structure was fabricated from thermoplastic polyurethane (TPU, Plastika Trcek d.o.o., Slovenia) with Shore hardness 90A, providing flexibility and high strain capability. The piezoresistive sensing elements were printed using conductive TPU filament (NinjaTek Eel, Fenner Precision Polymers, USA) with a volume resistivity of $1.5 \times 10^3\,\Omega\,\text{cm}$ and a Shore hardness of 90A.

The complete structure with embedded sensors was fabricated in a single process using MEX; detailed processing parameters are provided in Appendix 1. Electrical contacting of the 3D-printed embedded sensors consisted of applying conductive copper tape to the exposed contact pads on the corner sensors, soldering wire leads to the tape, and applying conductive silver

paste at the tape-sensor interface to reduce the contact resistance. This electrical contacting strategy has already been validated in previous research as a reliable interface [5, 36].

Multi-material interfaces in MEX introduce potential defects, including voids and weak interlayer bonding, that affect the sensor's performance. Interfacial adhesion between dissimilar thermoplastics depends on the material compatibility, with the solubility parameters and the coefficient of thermal expansion differences being the key predictors of bond strength [37]. The TPU and conductive TPU used in this work share a similar Shore hardness (90A), suggesting good material compatibility and interface formation. However, studies on TPU interfaces with conductive fillers have shown that interlaminar adhesion affects the mechanical integrity [38], which in turn influences the overall sensor reliability. Interface defects and manufacturing variability contribute to the signal noise and sensor-to-sensor response differences. The CNN-based approach compensates for this variability by learning directly from the actual sensor responses rather than relying on idealised material properties, making the system robust to manufacturing inconsistencies inherent in multi-material MEX.

2.2. Experiment and acquisition of training dataset

The structure was clamped in the fixation frame 3D-printed with black PLA filament (Plastika Trcek d.o.o., Slovenia) fixed to the steel support (see Figure 1(c)). The taps were applied manually using a modal hammer with an integrated piezoelectric force sensor (PCB Piezotronics, model 086C03) connected to the force input channel of the DAQ system (Dewesoft SIRIUS-X-16xACC, Dewesoft d.o.o., Slovenia). The four sensor wire-pairs were connected to individual voltage-divider circuits powered by a 12-V battery, with circuit outputs connected to the analog inputs of the DAQ system.

The taps were applied at 121 locations arranged in an 11×11 grid on the pad surface of $80 \times 80\,\text{mm}^2$ Figure 1(c). Three target force magnitudes (1 N, 2 N, 3 N) were applied using visual force feedback displayed on the PC, with the actual force being measured by the modal hammer load cell. Ten impacts were applied to each grid location for each force level, repeated across three DAQ sessions on separate days to capture the environmental variability, yielding a total dataset of $11 \times 11 \times 10 \times 3 \times 3 = 10890$ impact measurements.

A custom-script automated DAQ, processing, and storage, with each measurement recorded at a 50-kHz sampling rate for 0.3 second across six channels (four sensor voltage drops, supply voltage, and force signal). The sensor resistance was measured using the voltage divider:

$$R = \frac{(R_{ref} V_{out})}{(V_{supply} - V_{out})}, \tag{1}$$

where R_{ref} is the shunt resistance ($1800\,\Omega$), V_{out} is the acquired signal (output of the voltage divider), and V_{supply} is the supply voltage of the battery [39]. The static (DC) component of the measured signal V_{out} was removed by subtracting the mean value from the time series, isolating the dynamic resistance change. The processed data was automatically saved, with labels including normalised impact location coordinates ($X, Y \in [0, 1]$) and discrete force classes based on maximal tap force F_{max}. Force classes were defined as: class 0 for $F_{\text{max}} < 2\,\text{N}$, class 1 for $2\,\text{N} \leq F_{\text{max}} < 3\,\text{N}$, and class 2 for $F_{\text{max}} \geq 3\,\text{N}2\,\text{N} \leq F_{\text{max}} < 3\,\text{N}$. Automatic data storage ensured each measurement was accurately labeled for subsequent supervised learning.

The effect of the acquisition sample rate on the accuracy of the model was investigated. The best accuracy of the tap localisation was achieved with sample rates between 400 Hz and 1500 Hz. For this manuscript, the 1 kHz sample rate was used. Therefore, before the raw measurements were used for training, validation, and testing, the data was down-sampled from 50 kHz to 1 kHz. Signal down-sampling was performed using polyphase filtering to prevent aliasing artifacts [40]. Additionally, signals were truncated to 0.16 s, as longer acquisition intervals did not improve the localisation accuracy. No other pre-processing was applied to the data.

Representative sensor responses to taps with forces of 1 N and 3 N are presented in Figure 2, with five overlaid measurements illustrating signal repeatability and the raw signal characteristics that serve as neural network inputs.

2.3. Neural network

The neural network architecture consists of the 1-dimensional CNN encoder that extracts hierarchical features from the time-series sensor signals, producing a latent representation that is processed by two separate prediction heads for simultaneous tap-location regression and force classification (see Figure 3(a)).

The CNN architecture (encoder) was adapted from attention-enhanced 1D CNN methods, proven effective for noisy time-series sensor data [31].

The network input consists of four simultaneous time-series signals from the 3D-printed sensors (R in Equation

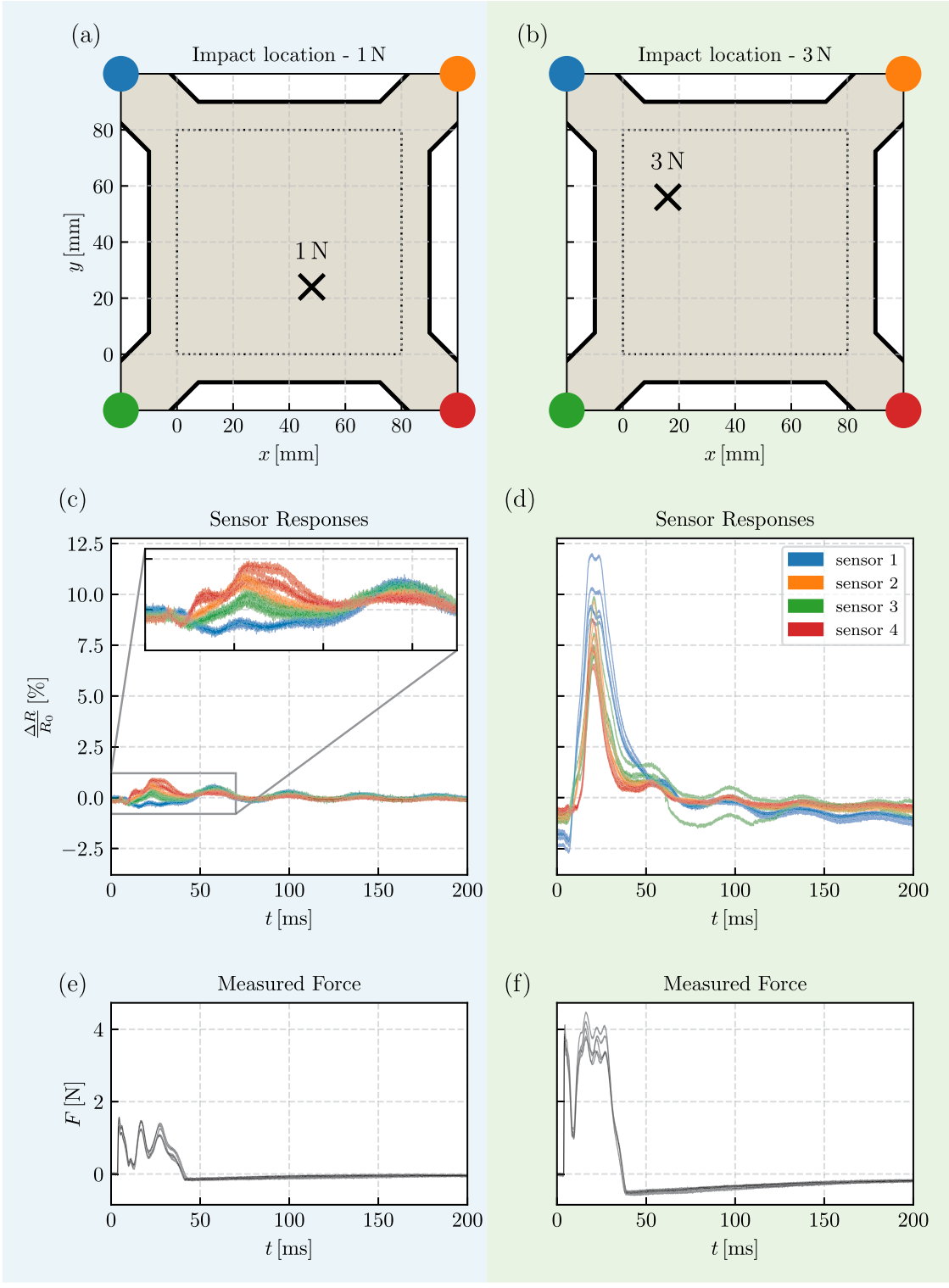

Figure 2. Raw signal characteristics from 3D-printed smart pad for five repeated impacts at the same location with 1 N (left column) and 3 N (right column) forces. (a,b) Impact location on the sensing region with colored sensors that correspond to line colors in the plots. (c,d) Four-channel resistance change responses. (e,f) Corresponding force measurements from modal hammer.

(1)), organised as a tensor of dimensions (B, C, T), where B is the batch size, C is the number of channels, and T is the number of time steps ($T = 0.16\,\text{s} \times 1\,\text{kHz} = 160$).

Feature extraction employs seven convolutional blocks that progressively down-sample the temporal dimension T while expanding the feature channels C,

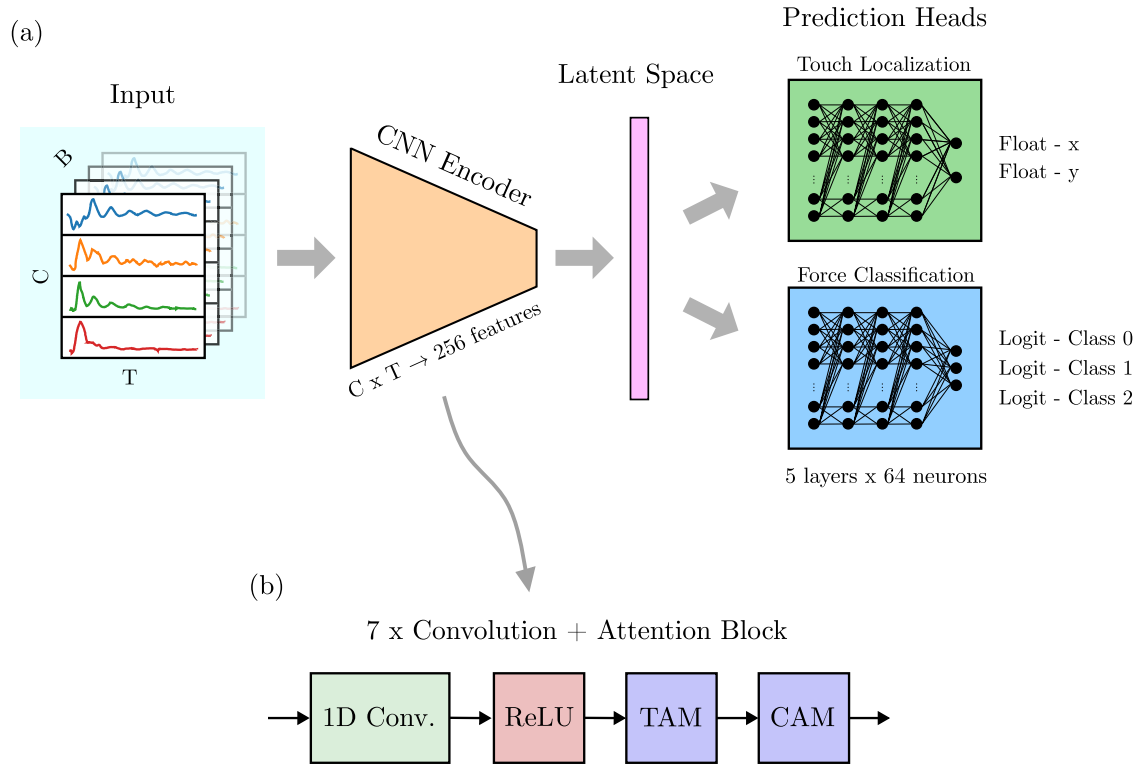

Figure 3. (a) Schematic of the model architecture with dual-head output for tap location and force prediction. (b) Structure of a single encoder block with 1D convolution, activation and time and channel attention.

extracting hierarchical representations from raw resistance signals to high-level impact descriptors Table 1.

Time Attention Modules (TAMs) and Channel Attention Modules (CAMs), adapted from [31], are integrated after each convolutional block to enhance the feature discrimination. TAM learns to emphasise the most informative temporal moments – impact arrival, peak response, and subsequent oscillations – while suppressing the baseline noise. CAM applies channel-wise attention to weight the feature maps produced by each convolutional layer, learning which extracted features – including those encoding sensor-specific characteristics – are most informative for localisation. Both modules use residual connections to preserve the original signal alongside attention-weighted features. This adaptive weighting accommodates the variable signal quality inherent to 3D-printed piezoresistive sensors. A detailed mathematical formulation is provided in [31].

Table 1. Data transformation through the 1D CNN encoder.

Layer	Convolutional Configuration[a]	Channel Transform	Time Transform[b]
1	$k=32, s=1$	$4 \rightarrow 32$	$T \rightarrow T$
2	$k=16, s=2$	$32 \rightarrow 32$	$T \rightarrow T/2$
3	$k=9, s=2$	$32 \rightarrow 64$	$T/2 \rightarrow T/4$
4	$k=6, s=2$	$64 \rightarrow 64$	$T/4 \rightarrow T/8$
5	$k=3, s=5$	$64 \rightarrow 128$	$T/8 \rightarrow T/40$
6	$k=3, s=5$	$128 \rightarrow 128$	$T/40 \rightarrow T/200$
7	$k=3, s=2$	$128 \rightarrow 256$	$T/200 \rightarrow T/400$
Global Pooling: $(256, T/400) \rightarrow (256)$			

[a] k = kernel size, s = stride [b] T = input time steps; $T = 160$ for this study (1 kHz sampling rate × 0.16 s duration; layer outputs are at least 1 sample)

The CNN (encoder) finishes with global average pooling across the temporal dimension, producing a 256-dimensional latent vector that compresses the extracted features.

Two prediction heads with identical fully-connected architectures process the latent representation: a contraction layer ($256 \rightarrow 64$), three hidden layers ($64 \rightarrow 64 \rightarrow 64$), and task-specific output layers. All the layers except the output layers use Rectified Linear Unit (ReLU) activation. The location head outputs two continuous values representing normalised impact coordinates (x, y) in the range 0 to 1. The force head outputs three class logits corresponding to force bins: low (0–2 N), medium (2–3 N), and high (>3 N). No activation functions are applied to the final output layers, providing raw values for mean squared error (location) and cross-entropy (force) loss computation.

The complete network contains 407,532 trainable parameters, enabling deployment on resource-constrained edge devices while maintaining computational efficiency for real-time usage.

The dataset was partitioned into training, validation, and test sets using an 80/10/10 random split, yielding 8,712 training, 1,089 validation, and 1,089 test samples.

A fixed random seed was used to ensure reproducibility of the data split. While samples from the same grid location can appear in different sets, each measurement represents a unique impact event with inherent variability in the applied force, timing, and environmental conditions across three separate DAQ sessions. This split strategy reflects the realistic deployment scenario where the system must generalise to impacts at known locations, and the measurement variability ensures no information leakage between sets.

The training objective employed a multi-task loss function with learnable task uncertainties [41] that automatically balances location-regression and force-classification objectives. The location loss $\mathcal{L}_{\text{MSE}}$ was computed as a mean squared error on normalised (x, y) coordinates. The force loss $\mathcal{L}_{\text{CE}}$ was computed as cross-entropy for three-class classification. Task weighting was implemented through learnable parameters s_{loc} and s_{force}, initialised to 0.0 and constrained to the range [-3, 3], which automatically balance the task contributions during training based on task uncertainty. The total loss function is given by:

$$\mathcal{L}_{\text{total}} = 0.5\, e^{-s_{\text{loc}}} \mathcal{L}_{\text{MSE}} + 0.5 s_{\text{loc}} + e^{-s_{\text{force}}} \mathcal{L}_{\text{CE}} + 0.5 s_{\text{force}} \quad (2)$$

where e is Euler's number.

The network was trained using the Adam optimiser [42] with momentum parameters $\beta_1 = 0.9$ and $\beta_2 = 0.999$, a constant learning rate of 2×10^{-4}, weight decay of 1×10^{-5}, and a batch size of 32.

Training was conducted for a maximum of 100 epochs with the validation loss computed after each epoch. Early stopping with patience of 7 epochs was applied based on the validation loss, with the lowest validation loss achieved at epoch 65, which defines the final model presented in the results (see the loss over epochs in Figure 4(a)).

Training was performed on an Nvidia RTX 5000 GPU using PyTorch with CUDA acceleration, requiring approximately 10 minutes of total training time.

3. Results

The results are presented in four parts: first, raw resistance signals from the 3D-printed sensors; second, neural network training convergence; third, impact localisation and force classification performance; and fourth, effect of sensor count reduction on accuracy.

Raw response Unprocessed signals from the 3D-printed sensors and force sensor of the modal hammer are presented in Figure 2. Differential sensing is evident, as the peak response amplitude varies with the impact proximity to each sensor (see Figure 2(c,d)). Peak resistance changes indicate force-dependent signal amplitude, with higher tap forces producing proportionally larger sensor responses (see Figure 2(c) vs. Figure 2(d)). High-frequency measurement noise is visible throughout the signals, reflecting the inherent limitations of 3D-printed piezoresistive elements, especially at low impact forces (see Figure 2(c)).

All four sensors respond to each impact with different amplitudes and temporal characteristics, capturing elastic wave propagation through the plate boundaries. Signals exhibit a rapid initial transient (<50 ms) followed by decaying oscillations and baseline drift.

These signal characteristics demonstrate that impact location and force information are encoded within the complex, multi-sensor response patterns, yet the combination of low signal-to-noise ratio, dispersive wave propagation, and nonlinear viscoelastic material properties renders analytical decoding approaches impractical, as discussed in Appendix 2.

Neural network convergence The total loss and split loss (localisation and force classification separate) plotted over epochs are shown in Figure 4(a,b), respectively. The total loss Figure 4(a) decreased smoothly from approximately 0.3 to −2.5 over 65 training epochs. The training and validation curves tracked closely throughout training, indicating minimal overfitting. The location loss (green) converged rapidly to near-zero, while the force loss (orange) plateaued around 0.02–0.05 Figure 4(b).

localisation and force-classification performance Error distribution Figure 4(c) follows the Rayleigh distribution with a mean localisation error of 3.56 mm, standard deviation of 2.61 mm, and 95th and 99th percentile errors of 7.20 mm and 12.57 mm, respectively. The regression model achieved an overall coefficient of determination (R^2) of 0.985 for coordinate prediction. The error distribution is heavily skewed toward small errors, with most predictions below 10 mm. The spatial error heatmap Figure 4(d) reveals a characteristic pattern: elevated error (≈6 mm) at the pad center and corners, with optimal accuracy (2–4 mm) in an intermediate annular region. This pattern reflects the differential information available across the sensing area. At the center, impacts produce similar amplitudes and arrival times at all four sensors, reducing the discriminative features. Near corners, one sensor dominates while others receive weak signals, yielding asymmetric inputs with limited inter-channel contrast. The intermediate ring provides balanced signal strengths across multiple sensors, maximising the differential information for localisation. Figure 4(f) demonstrates the prediction accuracy through a number-pad example, where

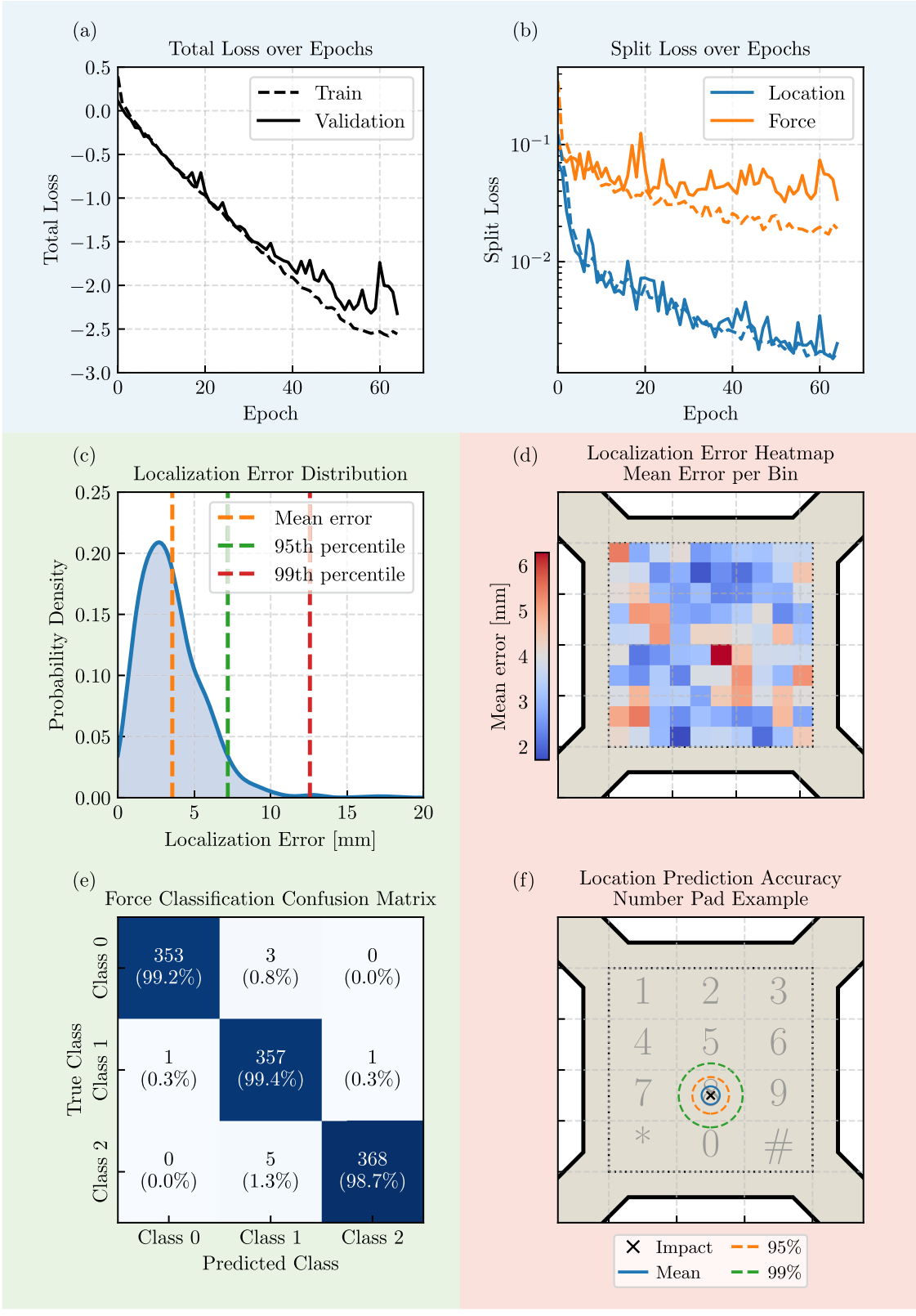

Figure 4. Neural network training and performance evaluation. (a) Total loss convergence. (b) Individual task losses for location and force prediction. (c) Distribution of localisation errors. (d) Spatial heatmap of localisation errors across the plate. (e) Confusion matrix for force classification. (f) Location prediction accuracy with error percentile circles with a number pad layout as an example application.

concentric circles represent the mean, 95th, and 99th percentile error radii. The 7.20-mm 95th percentile error enables reliable key identification in single-process 3D-printed number-pad applications, where the typical key spacing exceeds 15 mm.

The force classification results are presented in the confusion matrix (see Figure 4(e)). The overall classification accuracy ranged from 98.7% to 99.4% across all three force classes. Class 0 achieved 353/356 correct predictions (99.2%), Class 1 achieved 357/359 correct predictions (99.4%), and Class 2 achieved 368/373 correct predictions (98.7%). Confusion predominantly occurred between adjacent force levels, with 5 errors from Class 2 to Class 1. No cross-class confusion between Class 0 and Class 2 was observed, indicating effective force-level separation. Strong diagonal dominance with minimal off-diagonal values confirmed a robust force-classification performance.

Sensor-count reduction Here, the effect of the number of 3D-printed sensors used in the CNN on prediction accuracy is presented. Similar to the 4-sensor discussion above, the network was additionally trained with 3, 2, and single-sensor signals, omitting the remaining sensor channels from the input. Performance metrics for each sensor configuration are presented in Table 2.

A detailed performance comparison across sensor configurations is presented in Figure 5. All the sensor configurations achieved convergence within a similar number of epochs (see Figure 5(a–c)). The initial rate of total loss reduction was identical across configurations, with divergence occurring after approximately 10 epochs as sensor-limited configurations reached their performance ceiling Figure 5(a). Configurations with fewer sensors exhibited larger final total loss values, with the single-sensor case showing the most pronounced degradation. The location loss convergence rate degraded progressively with sensor reduction Figure 5(b), with the single-sensor configuration exhibiting distinctly slower learning during the critical 0-20 epoch period. In contrast, the force loss exhibited similar initial convergence rates across all the configurations, achieving comparable final values despite the sensor reduction Figure 5(c). Force classification accuracy remained above 98.6% for all the configurations, exhibiting negligible degradation (see Table 2). This asymmetry reveals that force information is encoded redundantly across the sensors, enabling the network to learn sufficiently discriminative features from individual sensors, while location prediction benefits from integrating differential timing and amplitude information from multiple sensors, demonstrating that the model learns distinct feature types for each task.

Table 2. Performance metrics as a function of sensor count.

Sensors	Mean (mm)	95th (mm)	99th (mm)	Force Acc (%)	R^2
4	3.562	7.195	12.571	99.08	0.985
3	4.455	9.310	15.538	98.90	0.976
2	5.692	12.331	18.408	98.62	0.963
1	6.320	13.498	23.016	98.81	0.951

In terms of location prediction, the mean localisation error increases from 3.56 mm (4 sensors) to 6.32 mm (1 sensor), while the 95th and 99th percentile accuracy decreases from 7.20 mm to 13.50 mm and from 12.57 mm to 23.02 mm, respectively Table 2. Progressive degradation with each removal of a sensor indicates that each additional sensor contributes meaningful spatial information Figure 5(d). No qualitative change in the spatial accuracy distribution pattern was observed–only the magnitude increased with sensor reduction. The accuracy circles expanded progressively with sensor reduction, with the 99th percentile (green) showing the most dramatic expansion Figure 5(e).

Sensor reduction resulted not only in a mean accuracy decrease but also in an increased prediction uncertainty, evident from wider error distributions Figure 5(d). The 99th percentile error degraded faster than the mean error, suggesting increased sensitivity to outliers with a reduced sensor count.

The 4-sensor configuration is justified for applications requiring higher accuracy (<4 mm mean error, <8 mm 95th percentile). A 2-sensor configuration represents a viable trade-off if an approximately 6-mm mean error is acceptable, offering a 50% reduction in DAQ channels, processing requirements, and system complexity. The force classification demonstrates a substantially lower sensitivity to sensor count than spatial localisation. The spatial error patterns remain predictable, regardless of the sensor count, enabling error-aware system design.

The contrasting degradation patterns (force classification maintains >98.6% accuracy with a single sensor while location error increases 77%) demonstrate that sensor requirements are task-dependent, enabling application-specific designs where force-only sensing uses minimal hardware while precision localisation justifies a multi-sensor configurations.

4. Discussion and conclusions

This work demonstrates that CNN-based processing transforms intentionally simple 3D-printed structures into accurate, functional smart systems. A flexible TPU pad with integrated piezoresistive elements was fabricated in a single process using commercially available materials and standard equipment. Despite a low signal quality characterised by poor sensitivity, low signal-to-noise ratio, and viscoelastic effects, the

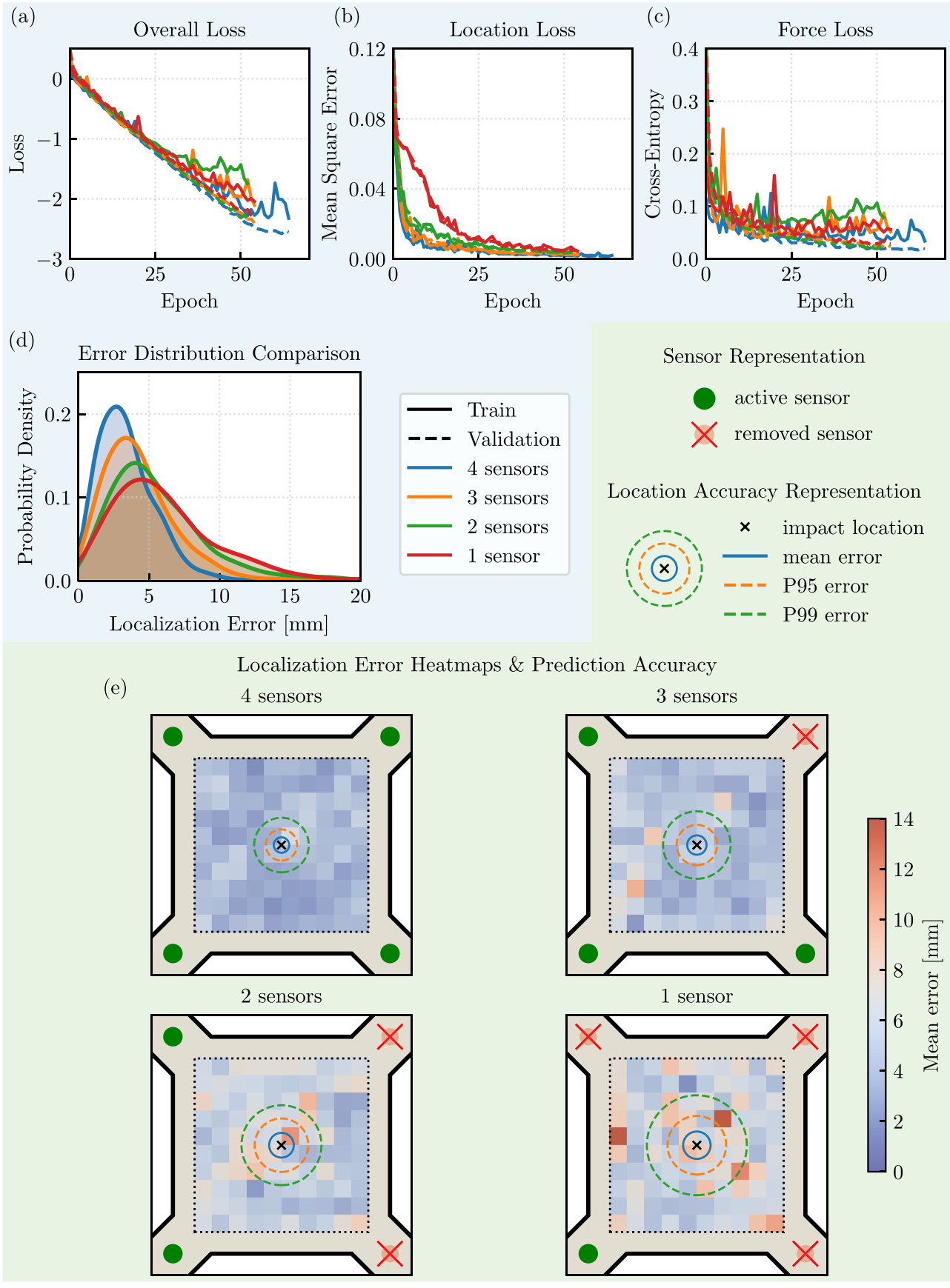

Figure 5. Performance comparison across sensor configurations (4, 3, 2, and 1 sensors). (a) Total loss convergence for all configurations. (b) Location loss convergence. (c) Force loss convergence. (d) Cumulative distribution function of localisation errors. (e) Spatial heatmaps of localisation errors for each sensor configuration with visualised prediction accuracy.

system achieves a 3.56-mm mean-localisation accuracy and >98.7% force-classification accuracy.

Sensor reduction from conventional multi-sensor configurations (typically 4–8 sensors) to 1–4 sensors reduces the multi-channel DAQ requirements, system cost and complexity. The 4-sensor configuration achieves competitive accuracy (3.56 mm), while the 1-sensor configuration demonstrates that functional performance persists (6.32 mm) under extreme hardware constraints (see comparison in Appendix 3). This establishes a paradigm where sensor quality and quantity are compensated by intelligent signal processing.

The methodology is applicable to human-machine interfaces [43], soft robotics [9, 44], pressure sensing [45], and structural health monitoring [46]. These fields benefit from the on-demand fabrication of application-specific geometries with embedded sensing in a single print process, where multi-material capabilities enable adjusting material selection to the application requirements and customised sensor placement without post-processing assembly.

Broader deployment requires addressing the current limitations in training requirements, hardware performance, and system characterisation. The CNN is geometry-specific: training data must match the sensor configuration, and material or structural changes necessitate retraining. Signal quality is constrained by the piezoresistive elements, while long-term stability, environmental robustness, and sensor drift remain uncharacterised.

Future work targets these constraints through complementary strategies. Transfer learning [47] and physics-informed neural networks [48] offer pathways toward cross-geometry deployment with reduced data requirements. Hardware improvements – optimiser sensor geometry [16, 49], electromagnetic shielding [12], and enhanced signal conditioning – can improve input signal quality. Ensemble methods [50] combined with data augmentation [51] may reduce the prediction variance. Field validation is required to characterise the long-term behaviour before deployment. Addressing these aspects would extend the methodology from laboratory demonstration to practical application.

Acknowledgments

The authors acknowledge the use of Claude Sonnet 4.5 (Anthropic) for assistance with grammar correction and language refinement of the manuscript.

Author contributions

CRediT: **Tibor Barši Palmić:** Conceptualization, Data curation, Formal analysis, Investigation, Methodology, Software, Validation, Visualization, Writing – original draft, Writing – review & editing; **Enej Podlipnik:** Data curation, Formal analysis, Investigation, Methodology, Software, Visualization, Writing – original draft; **Janko Slavič:** Conceptualization, Funding acquisition, Investigation, Methodology, Project administration, Resources, Supervision, Validation, Writing – review & editing.

Data availability

Both the dataset and `Python` code for the CNN model are available on a public GitHub repository [35].

Disclosure statement

No potential conflict of interest was reported by the author(s).

Funding

The authors acknowledge the partial financial support from the Slovenian Research Agency (research core funding No. P2-0263 and research project L2-60140).

ORCID

Tibor Barši Palmić https://orcid.org/0000-0001-6403-8233
Janko Slavič http://orcid.org/0000-0002-5982-8377

References

[1] Kanishka K, Acherjee B. Revolutionizing manufacturing: a comprehensive overview of additive manufacturing processes, materials, developments, and challenges. J Manuf Process. 2023;107:574–619. https://doi.org/10.1016/j.jmapro.2023.10.024
[2] Bodaghi M, Wang L, Zhang F, et al. 4D printing roadmap. Smart Mater Struct. 2024;33:113501. https://doi.org/10.1088/1361-665X/ad5c22
[3] Dijkshoorn A, Werkman P, Welleweerd M, et al. Embedded sensing: integrating sensors in 3-D printed structures. J Sens Sens Syst. 2018;7:169–181. https://doi.org/10.5194/jsss-7-169-2018
[4] Ren H, Yang X, Wang Z, et al. Smart structures with embedded flexible sensors fabricated by fused deposition modeling-based multimaterial 3D printing. Int J Smart Nano Mater. 2022;13:447–464. https://doi.org/10.1080/19475411.2022.2095454
[5] Košir T, Slavič J. Single-process fused filament fabrication 3D-printed high-sensitivity dynamic piezoelectric sensor. Addit Manuf. 2022;49:102482. https://doi.org/10.1016/j.addma.2021.102482
[6] Tao R, Shi J, Granier F, et al. Multi-material fused filament fabrication of flexible 3D piezoelectric nanocomposite lattices for pressure sensing and energy harvesting applications. Appl Mater Today. 2022;29:101596. https://doi.org/10.1016/j.apmt.2022.101596
[7] Xiang D, Zhang X, Han Z, et al. 3D printed high-performance flexible strain sensors based on carbon nanotube and graphene nanoplatelet filled polymer composites.

J Mater Sci. 2020;55:15769–15786. https://doi.org/10.1007/s10853-020-05137-w

[8] Arh M, Slavič J. Single-process 3D-printed triaxial accelerometer. Adv Mater Technol. 2022;7:2101321. https://doi.org/10.1002/admt.202101321

[9] Wei Y, Li B, Domingos M, et al. Fully 3D printed flexible, conformal and multi-directional tactile sensor with integrated biomimetic and auxetic structure. Commun Eng. 2023;2(1). https://doi.org/10.1038/s44172-023-00131-x

[10] Arh M, Slavič J, Boltežar M. Experimental identification of the dynamic piezoresistivity of fused-filament-fabricated structures. Addit Manuf. 2020;36:101493. https://doi.org/10.1016/j.addma.2020.101493

[11] Stano G, Bottiglione F, Percoco G. Fused filament fabrication for one shot additive manufacturing of capacitive force sensors. Procedia CIRP. 2022;110:168–173. https://doi.org/10.1016/j.procir.2022.06.031

[12] Košir T, Slavič J. Manufacturing of single-process 3D-printed piezoelectric sensors with electromagnetic protection using thermoplastic material extrusion. Addit Manuf. 2023;73:103699. https://doi.org/10.1016/j.addma.2023.103699

[13] Stano G, Sayah N, Smith DE, et al. Effect of process parameters in additively manufactured sensors prepared via material extrusion processes: correlation among electrical, mechanical and microstructure properties. Addit Manuf Lett. 2024;9:100194. https://doi.org/10.1016/j.addlet.2024.100194

[14] Nowka M, Ruge K, Schulze L, et al. Characterization of the anisotropic electrical properties of additively manufactured structures made from electrically conductive composites by material extrusion. Polymers. 2024;16(20):2891. https://doi.org/10.3390/polym16202891

[15] Yang Y, Tang Y, Xue K, et al. Adaptive 3D printing of moldable conductive polymer composite for highly sensitive soft sensors with a broad working range. npj Flex Electron. 2026;10(1):22. https://doi.org/10.1038/s41528-025-00523-3

[16] Stano G, Pavone A, Jafor MA, et al. Enhancing the sensitivity of 3D printed sensors via ironing and void reduction. Virtual Phys Prototyp. 2024;19:e2331153. https://doi.org/10.1080/17452759.2024.2331153

[17] Dhinesh SK, Lakshmanan SKK, Pitchandi N. Influence of substrate material and sensor geometry variations on the performance of fused deposition modeling-printed strain sensors. 3D Print Addit Manuf. 2025;12:373–389. https://doi.org/10.1089/3dp.2023.0320

[18] Stano G, Ovy SMI, Edwards JR, et al. One-shot additive manufacturing of robotic finger with embedded sensing and actuation. Int J Adv Manuf Technol. 2022;124:467–485. https://doi.org/10.1007/s00170-022-10556-x

[19] Zolfagharian A, Kaynak A, Kouzani A. Closed-loop 4D-printed soft robots. Mater Des. 2020;188:108411. https://doi.org/10.1016/j.matdes.2019.108411

[20] Ciampa F, Meo M, Barbieri E. Impact localization in composite structures of arbitrary cross section. Struct Health Monit. 2012;11:643–655. https://doi.org/10.1177/1475921712451951

[21] Bulletti A, Merlo EM, Capineri L. Analysis of the accuracy in impact localization using piezoelectric sensors for structural health monitoring with multichannel real-time electronics. In: 2020 IEEE International Workshop on Metrology for AeroSpace, MetroAeroSpace 2020 – Proceedings; 2020. p. 480–484. doi: 10.1109/MetroAeroSpace48742.2020.9160275

[22] Damm AM, Spitzmüller C, Raichle AT, et al. Deep learning for impact detection in composite plates with sparsely integrated sensors. Smart Mater Struct. 2020;29:125014. https://doi.org/10.1088/1361-665X/abb644

[23] Li S, Peng G, Yuan H, et al. Robust data-driven structural impact localization with multisensor real-time monitoring. IEEE Sens J. 2024;24:1644–1654. https://doi.org/10.1109/JSEN.2023.3326961

[24] Xu Q. Impact detection and location for a plate structure using least squares support vector machines. Struct Health Monit. 2014;13:5–18. https://doi.org/10.1177/1475921713495083

[25] Lamberti A, Luyckx G, Paepegem WV, et al. Detection, localization and quantification of impact events on a stiffened composite panel with embedded fiber bragg grating sensor networks. Sensors (Switzerland). 2017;17(4):743. https://doi.org/10.3390/s17040743

[26] Merlo EM, Bulletti A, Giannelli P, et al. A novel differential time-of-arrival estimation technique for impact localization on carbon fiber laminate sheets. Sensors (Switzerland). 2017;17(10):2270. https://doi.org/10.3390/s17102270

[27] Du L, Jiang W, Luo Z, et al. Multi FBG sensor-based impact localization with a hybrid correlation interpolation method. Meas Sci Technol. 2022;33:75002. https://doi.org/10.1088/1361-6501/ac5d76

[28] Zhu J, Ho SCM, Kong Q, et al. Estimation of impact location on concrete column. Smart Mater Struct. 2017;26:55037. https://doi.org/10.1088/1361-665X/aa6768

[29] Kiranyaz S, Avci O, Abdeljaber O, et al. 1D convolutional neural networks and applications: a survey. Mech Syst Signal Process. 2021;151:107398. https://doi.org/10.1016/j.ymssp.2020.107398

[30] Chien JT, Chen YH. Learning continuous-time dynamics with attention. IEEE Trans Pattern Anal Mach Intell. 2023;45:1906–1918. https://doi.org/10.1109/TPAMI.2022.3162711

[31] Xu H, Tian Y, Ren H, et al. A lightweight channel and time attention enhanced 1D CNN model for environmental sound classification. Expert Syst Appl. 2024;249:123768. https://doi.org/10.1016/j.eswa.2024.123768

[32] Fu H, Xu Q. Locating impact on structural plate using principal component analysis and support vector machines. Math Prob Eng. 2013;2013:352149. https://doi.org/10.1155/2013/352149

[33] Ribeiro F, Possetti GRC, Fabris JL, et al. Smart optical fiber sensor for impact localization on planar structures. In: SBMO/IEEE MTT-S International Microwave and Optoelectronics Conference Proceedings; 2013. p. 1–3. https://doi.org/10.1109/IMOC.2013.6646418

[34] Migot A, Saaudi A, Giurgiutiu V. New method of impact localization on plate-like structures using deep learning and wavelet transform. Sensors. 2025;25(6):1926. https://doi.org/10.3390/s25061926

[35] Barši Palmić T, Podlipnik E, Slavič J. Single-process 3D-printed smart pad: neural network model and dataset;

2025. Available from: https://github.com/ladisk/papers/tree/master/3D-Printed-Smart-Pad.
[36] Palmić TB, Slavič J. Single-process 3D-printed stacked dielectric actuator. Int J Mech Sci. 2022;230:107555. https://doi.org/10.1016/j.ijmecsci.2022.107555
[37] Richter F, Wu D. Interfacial adhesion between dissimilar thermoplastics fabricated via material extrusion-based multi-material additive manufacturing. Mater Des. 2025;252:113688. https://doi.org/10.1016/j.matdes.2025.113688
[38] Goh GL, Lee S, Cheng SH, et al. Enhancing interlaminar adhesion in multi-material 3D printing: a study of conductive PLA and TPU interfaces through fused filament fabrication. Mater Sci Addit Manuf. 2024;3(1):2672. https://doi.org/10.36922/msam.2672
[39] Palmić TB, Slavič J, Boltežar M. Process parameters for fff 3d-printed conductors for applications in sensors. Sensors (Switzerland). 2020;20:1–21. https://doi.org/10.3390/s20164542
[40] Virtanen P, Gommers R, Oliphant TE, et al. SciPy 1.0: fundamental algorithms for scientific computing in Python. Nat Methods. 2020;17:261–272. https://doi.org/10.1038/s41592-019-0686-2
[41] Cipolla R, Gal Y, Kendall A. Multi-task learning using uncertainty to weigh losses for scene geometry and semantics. In: Proceedings of the IEEE Computer Society Conference on Computer Vision and Pattern Recognition; 2018. p. 7482–7491. https://doi.org/10.1109/CVPR.2018.00781
[42] Kingma DP, Ba JL. Adam: a method for stochastic optimization. In: 3rd International Conference on Learning Representations, ICLR 2015 – Conference Track Proceedings; 2015. https://doi.org/10.48550/arXiv.1412.6980
[43] Dezaki ML, Zolfagharian A, Demoly F, et al. Human–material interaction enabled by fused filament fabrication 4D printing. Adv Eng Mater. 2024;26:2301917. https://doi.org/10.1002/adem.202301917
[44] Khalid MY, Arif ZU, Ahmed W, et al. 4D printing: technological developments in robotics applications. Sens Actuators A: Phys. 2022;343:113670. https://doi.org/10.1016/j.sna.2022.113670
[45] Massaroni C, Vitali L, Lo Presti D, et al. Fully additively 3D manufactured conductive deformable sensors for pressure sensing. Adv Intell Syst. 2024;6:2300901. https://doi.org/10.1002/aisy.202300901
[46] Ferreira PM, Machado MA, Carvalho MS, et al. Embedded sensors for structural health monitoring: methodologies and applications review. Sensors. 2022;22(21):8320. https://doi.org/10.3390/s22218320
[47] Yu F, Xiu X, Li Y. A survey on deep transfer learning and beyond. Mathematics. 2022;10(19):3619. https://doi.org/10.3390/math10193619
[48] Raissi M, Perdikaris P, Karniadakis GE. Physics-informed neural networks: a deep learning framework for solving forward and inverse problems involving nonlinear partial differential equations. J Comput Phys. 2019;378:686–707. https://doi.org/10.1016/j.jcp.2018.10.045
[49] Imranuddin S, Singh AP, Stano G, et al. Enhancing 3-D-printed piezoresistive sensors: an investigation into process parameters, sensor geometries and materials selection. IEEE Sens J. 2025;25:13063–13072. https://doi.org/10.1109/JSEN.2025.3546641
[50] Ganaie MA, Hu M, Malik AK, et al. Ensemble deep learning: a review. Eng Appl Artif Intell. 2022;115:105151. https://doi.org/10.1016/j.engappai.2022.105151
[51] Wen Q, Sun L, Yang F, et al. Time series data augmentation for deep learning: a survey. In: IJCAI International Joint Conference on Artificial Intelligence, aug, California; International Joint Conferences on Artificial Intelligence Organization; 2021. p. 4653–4660. https://doi.org/10.24963/ijcai.2021/631
[52] Hassani S, Dackermann U. A systematic review of advanced sensor technologies for non-destructive testing and structural health monitoring. Sensors. 2023;23(4):2204. https://doi.org/10.3390/s23042204
[53] Meng W, Xiao W. Energy-based acoustic source localization methods: a survey. Sensors. 2017;17(2):376. https://doi.org/10.3390/s17020376
[54] Philibert M, Yao K, Gresil M, et al. Lamb waves-based technologies for structural health monitoring of composite structures for aircraft applications. Eur J Mater. 2022;2:436–474. https://doi.org/10.1080/26889277.2022.2094839
[55] Kundu T, Nakatani H, Takeda N. Acoustic source localization in anisotropic plates. Ultrasonics. 2012;52:740–746. https://doi.org/10.1016/j.ultras.2012.01.017
[56] Merlo EM, Bulletti A, Bertoni F, et al. Analysis of errors in the estimation of impact positions in plate-like structures through the triangulation formula. Sensors. 2018;18(10):3426. https://doi.org/10.3390/s18103426
[57] Singh SK, Fakih MA, Malinowski PH. Damage detection and localization based on different types of actuators using the electromechanical impedance method in 3d-printed material. Smart Mater Struct. 2023;32:115004. https://doi.org/10.1088/1361-665X/acfa7e
[58] Liu Q, Wang F, Li J, et al. A hybrid support vector regression with multi-domain features for low-velocity impact localization on composite plate structure. Mech Syst Signal Process. 2021;154:107547. https://doi.org/10.1016/j.ymssp.2020.107547
[59] Xiao D, de Sá Rodrigues F, Sharif-Khodaei Z, et al. A general probabilistic framework for impact localisation based on flexural wave propagation. Mech Syst Signal Process. 2025;226:112320. https://doi.org/10.1016/j.ymssp.2025.112320
[60] Coles A, de Castro BA, Andreades C, et al. Impact localization in composites using time reversal, embedded pzt transducers, and topological algorithms. Front Built Environ. 2020;6:27. https://doi.org/10.3389/fbuil.2020.00027

Appendix

Appendix 1. 3D printing process details

Table A1 summarises the fabrication parameters used for the structure.

The multi-toolhead printer configuration was selected for its independent extruder capability. Separate extruders prevent cross-contamination between the conductive and non-conductive materials, which would otherwise compromise sensor electrical isolation. This commercially available, unmodified system enables single-process, multi-material fabrication without manual intervention.

Processing parameters were selected based on TPU material requirements and interface quality considerations. Low print speeds (15–40 mm/s) are necessary for TPU processing due to its flexible nature, and slower speeds improve the interlayer adhesion and interface quality between dissimilar materials. The 100% rectilinear infill produces a solid structure required for mechanical integrity and consistent elastic wave propagation throughout the sensing medium. Identical parameters were applied to both the TPU and conductive TPU because both materials share similar Shore hardness (90A), enabling compatible co-processing with a simplified workflow. The 225°C nozzle temperature falls within the standard TPU processing window and provides adequate material flow without thermal degradation.

Table A1. Processing parameters for MEX fabrication of the structure.

Parameter	Value
3D Printer	Original Prusa XL (5-toolhead configuration)
Manufacturer	Prusa Research a.s., Czech Republic
Process	Material extrusion (MEX) per ISO/ASTM 52900
Nozzle diameter	0.4 mm
Layer height	0.2 mm
Nozzle temperature	225°C
Bed temperature	50°C
Perimeter speed	40 mm/s
Infill speed	40 mm/s
Infill pattern	100% rectilinear

Appendix 2. Traditional impact-localisation methods

Impact-localisation methods developed for structural health monitoring typically employ calibrated piezoelectric transducers on metallic or composite aerospace structures [46, 52]. These methods rely on assumptions that are systematically violated by the 3D-printed flexible sensor system presented in this work.

Energy-based methods estimate the impact location from amplitude ratios, assuming acoustic energy decays predictably with distance according to geometric spreading laws [53]. Reliable application requires calibrated sensors with known sensitivity and homogeneous material properties [21]. The 3D-printed piezoresistive sensors exhibit manufacturing variability in conductive TPU deposition, producing differing response characteristics across sensor elements [14]. Viscoelastic materials such as TPU introduce frequency-dependent damping that causes amplitude patterns to deviate from simple decay models [54].

Time-of-arrival triangulation methods require accurate detection of the wave arrival times at multiple sensors, with standard acoustic emission systems employing sampling rates of 500 kHz to 5 MHz [55]. This requires specialised DAQ hardware and presents high computational demands for the amount of data that is acquired, which is a limiting factor for real-world applications of 3D-printed structures. Beyond sampling limitations, triangulation assumes a known, constant wave velocity [20]. Flexural waves in thin flexible plates exhibit strong dispersion, with velocity dependent on frequency [56], which introduces fundamental ambiguity in arrival-time determination.

Classical localisation approaches were evaluated on the present dataset. These methods achieved substantially higher localisation errors than the CNN approach, confirming they are not well-suited to the 3D-printed flexible sensor system.

These incompatibilities between classical method assumptions and the physical characteristics of the flexible sensor system motivated the machine-learning approach. Rather than relying on precise timing measurements or calibrated amplitude relationships, the CNN learns spatial patterns directly from complete signal waveforms, accommodating the material variability and dispersive wave propagation inherent to the system.

Appendix 3. Comparison with impact-localisation methods

Table A2 summarises impact-localisation methods from recent literature, comparing experimental setup, method requirements, and localisation accuracy. To enable direct comparison across different plate geometries, accuracy is normalised as a percentage of the plate diagonal.

The extended comparison in Table A2 positions this work among recent impact-localisation studies. Singh et al. [57] represents the only other investigation of 3D-printed materials, achieving 4.48 mm accuracy on ABS using electromechanical impedance with surface-bonded sensors (not 3D-printed). In contrast, the present work achieves comparable accuracy (3.56 mm vs 4.48 mm) on a smaller plate with fully integrated sensors manufactured during the printing process, eliminating post-fabrication sensor bonding. Among studies using four sensors, Liu et al. [58] reported a 4.14-mm average error on CFRP using support vector regression with 140 hand-crafted features, while the CNN approach presented here achieves comparable accuracy through end-to-end learning without manual feature engineering. Physics-based methods such as Xiao et al. [59] and Coles et al. [60] require a wave-velocity characterisation or baseline signal acquisition, achieving 6.7–15.3 mm and 10.7 mm, respectively, on rigid composite substrates.

Table A2. Comparison of impact localisation methods.

Ref	Method	Plate	Sensors	Requirements	Highest Accuracy	Accuracy (% diag.)
This work	CNN+Attention, regression	100×100 mm, TPU	4 piezoresistive	1 kHz, ~8,700 training impacts, no calibration	3.56 mm mean	2.5%
[57] (2023)	EMI, regression	200×200 mm, 3D-printed ABS	2 PZT + 1 MFC	1–500 kHz scan, surface-bonded sensors	4.48 mm	1.6%
[58] (2021)	BA-SVR, regression	240×240 mm, CFRP	4 FBG	5-kHz sampling rate, multi-domain features, bat algorithm optimisation	4.14 mm avg	1.2%
[59] (2025)	Bayesian/MCMC, regression	290–475 mm, CFRP/sandwich	4 PZT	2-MHz sampling rate, Flexural wave model, velocity characterisation	6.7–15.3 mm	1.6–2.9%
[60] (2020)	Time reversal	200×200 mm, CFRP	4 embedded PZT	2-MHz sampling rate, baseline signals	10.7 mm	3.8%
[23] (2024)	EMD+MSVR, regression	300×300 mm, acrylic	4 PZT	100 kHz, wavelet denoising	6.31 ± 1.74 mm	1.5%
[22] (2020)	CNN+STFT, classification†	280×280 mm, CFRP	3 MEMS/PZT	500 kHz, 21k training impacts, STFT	99.8%, 0.3 mm dev.	N/A†
[34] (2025)	CNN+wavelet, classification†	900×500 mm, aluminum	4 PWAS	5 MHz, wavelet segmentation	99–100%	N/A†

Notes: Accuracy (% diag.) = mean error / plate diagonal × 100. †Classification methods predict discrete regions rather than continuous coordinates; % diagonal is N/A.

Methods: CNN = convolutional neural network; EMI = electromechanical impedance; BA-SVR = bat algorithm support vector regression; MCMC = Markov chain Monte Carlo; EMD = empirical mode decomposition; MSVR = multi-output support vector regression; STFT = short-time Fourier transform.

Materials: TPU = thermoplastic polyurethane; ABS = acrylonitrile butadiene styrene; CFRP = carbon fiber reinforced polymer.

Sensors: PZT = lead zirconate titanate; MFC = macro fiber composite; FBG = fiber Bragg grating; MEMS = microelectromechanical systems; PWAS = piezoelectric wafer active sensor.